

Science Arts & Métiers (SAM)

is an open access repository that collects the work of Arts et Métiers ParisTech researchers and makes it freely available over the web where possible.

This is an author-deposited version published in: <http://sam.ensam.eu>
Handle ID: <http://hdl.handle.net/10985/8356>

To cite this version :

Brahim TLILI, Corinne NOUVEAU, M.J WALOCK, M. NASRI, T. GHRIB - Effect of layer thickness on thermal properties of multilayer thin films produced by PVD - Vacuum - Vol. 86, n°8, p.1048-1056 - 2012

Any correspondence concerning this service should be sent to the repository

Administrator : archiveouverte@ensam.eu

Effect of layer thickness on thermal properties of multilayer thin films produced by PVD

B. Tlili ^{a,b,*}, C. Nouveau ^b, M.J. Walock ^{a,c}, M. Nasri ^a, T. Ghrib ^d

^aUR Mécanique Appliquée, Ingénierie et Industrialisation (M.A.2I), ENIT, BP 37, Le Belvédère, 1002 Tunis, Tunisia

^bLaboratoire Bourguignon des Matériaux et Procédés (LaBoMaP), Centre Arts et Métiers ParisTech de Cluny, Rue Porte de Paris, F-71250 Cluny, France

^cDepartment of Physics, University of Alabama at Birmingham, USA

^dPhotothermal Laboratory, I PEI 8000 Nabeul, Tunisia

A B S T R A C T

Cr/CrN/CrAlN, CrN/CrAlN and Cr/CrN thin layers were deposited by PVD (Physical Vapor Deposition). The multilayers were obtained from the combined deposition of different layers Cr, CrN and CrAlN thick films on on AISI4140 steel and silicon substrates at 200 °C, and evaluated with respect to fundamental properties such as structure and thermal properties. Cr, CrN and CrAlN single layers were also prepared for comparison purposes. The structural and morphological properties of PVD layers were characterized by X-ray diffraction (XRD) and scanning electron microscopy (SEM) coupled with EDS + WDS micro-analyses, stresses were determined by the Newton's rings methods using the Stoney's equation and surface hardening and hardness profiles were evaluated by micro hardness measurements. The XRD data and HRTEM showed that both the Cr/CrN, CrN/CrAlN and Cr/CrN/CrAlN multilayer coatings exhibited B1NaCl structure with a prominent reflection along (200) plane, and CrAlN sub-layer microstructures composed of nanocrystallites uniformly embedded in an amorphous matrix. The innovation of this work was to use the thickness of three different coating types to determine the thermal properties. Furthermore, an empirical equation was developed for the thermal properties variations with temperature of AISI4140 steel coated with different multilayer coatings. The thermal conductivity of CrAlN single layered was lower than the multilayer and the bulk material AISI4140. Moreover, the influences of structure and composition of the multilayer coatings on the thermal properties are discussed.

The thermal conductivity of nanoscale thin film is remarkably lower than that of bulk materials because of its various size effects.

Keywords:

Multilayers Cr/CrN/CrAlN

Thermal conductivity

PVD

Model

1. Introduction

Thin films based on carbides and nitrides of transition metals have been very successful in improving the performance of cutting tools. Although TiN is the most widely used in industrial applications, CrN has been gaining importance in recent years due to its superior corrosion and wear resistance, friction behavior and low internal stress [1–3]. However, there are an increasing number of applications where properties of single layer coatings are not sufficient. Recent research is focused on the development of nanolayered multilayer coatings in order to meet the requirements in terms of hardness, thermal stability, coefficient of friction, corrosion resistance and internal stress [4–11]. Nanolayered

multilayer coatings are composed of two or three different layers at the nanometer scale. The bilayers of the multilayers can be metals, carbides, nitrides or oxides of different materials or a combination of one layer made of nitride, carbide or oxide of one metal and the second layer made of another metal. A variety of multilayer systems such as TiN/CrN [4,5], TiAlN/CrN [6,7], TiN/NbN [8–11], etc., have been studied extensively. However, there are very few reports on the multilayer coatings based on CrN and CrAlN [12]. CrN films have been used for cutting tools, molding dyes and machine parts. But the oxidation resistance of CrN is limited up to 800 °C [13]. For hard protective coatings, thermal stability is a main property as they are exposed to high temperatures during the cutting process. The addition of Al to CrN system permits to work at higher temperatures where the oxidation occurs [14]. CrAlN coatings have been reported to be stable up to a temperature of 900 °C depending upon the Al content in the coatings [15]. CrAlN coatings also exhibit higher hardness and a lower friction coefficient compared to CrN coatings [16,17]. The structural and thermal properties have been

* Corresponding author. Laboratoire Bourguignon des Matériaux et Procédés (LaBoMaP), Centre Arts et Métiers ParisTech de Cluny, Rue Porte de Paris, F-71250 Cluny, France. Tel.: +33 (06) 85 30 58 95.

E-mail address: tlili_brahim@yahoo.fr (B. Tlili).

studied by X-ray diffraction (XRD), photo-thermal deflection (PTD) technique [18–20].

2. Experimental details

The substrate material used in the present study was commercial AISI 4140 steel with the composition presented in Table 1. The substrates were hardened and tempered to a hardness of 4.5 HV_{0.05}. They were ground, polished and cleaned with trichloroethylene, acetone and alcohol in an ultrasonic cleaner.

2.1. Coatings deposition and characterizations

The multilayers were deposited on mechanically polished steel (AISI4140), with a surface roughness $R_a = 0.2 \mu\text{m}$ and silicon $10 \times 10 \text{ mm}^2$ (for internal stress and thickness measurements) SiO_2 $10 \times 10 \text{ mm}^2$ substrates by using a dual RF magnetron sputtering system (NORDIKO type 3500-13, 56 MHz) equipped with two targets of high purity (Cr of 99.995% and Al of 99.999%) as shown in Fig. 1, the working pressure is 0.4 μbar . Before deposition, the substrates and the targets were ultrasonically cleaned and etched in pure argon plasma for 5 min. The deposition conditions such as target power, bias voltage, and deposition time are given in Table 2. The deposition temperature was around 200 °C. Very high purity nitrogen (N_2 of 99.9999%) was introduced into the vacuum chamber as the reactive gas. The residual pressure was 10^{-7} mbar. In both cases, the targets were 101.6 mm of diameter and 3 mm thick. The substrate/target distance was 80 mm.

The Cr/CrN or Cr/CrN/CrAlN multilayers can be defined as graded coatings. Actually, the CrN or CrAlN layers were achieved after decreasing the argon concentration inside the deposition chamber from 100% to 80%, and increasing the nitrogen content to 20%.

The morphology, thickness and the composition of the coatings were determined by Scanning Electron Microscopic observations (SEM) and EDS + WDS microanalyses (Jeol JSM-5900 LV). XRD analyses (SIEMENS D500, Co-K_(radiation)) permitted the determination of the crystalline orientations of the layers.

The residual stresses (σ) were determined by interferometer (Newton's rings method [21]) by the measurement of the curvature radius (R_0 , R) of the Si (100) specimens before and after deposition and calculated with the Stoney's equation [21,22]:

$$\sigma = \frac{1}{6} \left(\frac{E_s}{(1 - \nu_s)} \right) \left(\frac{t_s^2}{t_f} \right) \left(\frac{1}{R} - \frac{1}{R_0} \right) \quad (1)$$

where E_s and ν_s are Young's modulus (181 GPa) and Poisson's ratio (0.28) of silicon (100), respectively [17]. The $(E_s/(1 - \nu_s))$ term is the biaxial modulus of the Si (100) substrate ($E = 1.805 \times 10^{11} \text{ N/mm}^2$). Both t_s and t_f are the thicknesses of the Si substrate and of the layer, respectively, while R_0 and R are the curvature radius before and after deposition, respectively.

2.2. Photo-thermal deflection (PTD)

The thermal properties are determined by photo-thermal deflection (PTD) [23,24] which is a non-destructive technique. In

Table 1
Chemical composition of AISI4140 steel.

Element	Content (%)
C	0.410
Mn	0.770
Si	0.280
S	0.026
Cr	1.020
P	0.019
Mo	0.160

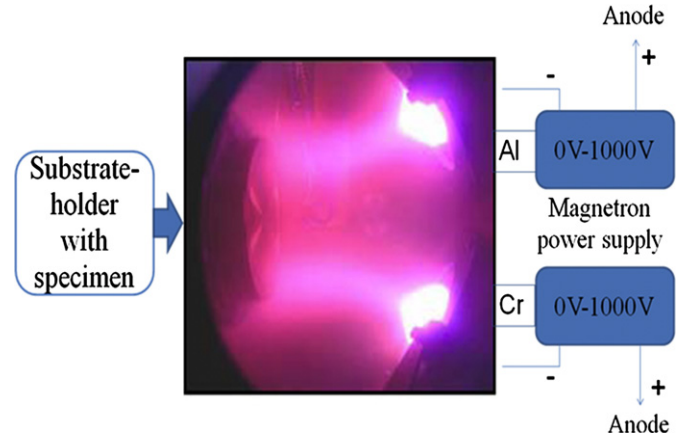


Fig. 1. Plasmas operated in the magnetron.

this work we used this technique in order to determine the local thermal properties of a stacking formed with succession of thin layers described above (Section 2.1). We proceeded by determining the thermal conductivity and thermal diffusivity of a single layer of Cr deposited on the substrate then, thermal properties of the bilayers of Cr/CrN and multilayer Cr/CrN/CrAlN are determined using a mathematical model and an appropriate experimental setup.

2.2.1. Experimental setup

The PTD setup developed in our laboratory as shown in Fig. 2. It has been applied here to study the photo-thermal signal; the sample is heated by a light from a 100 W power halogen lamp with power modulated thanks to a mechanical chopper at a variable frequency. A He-Ne laser probe beam of diameter $d = 100 \mu\text{m}$, skimming the sample surface at a distance z , is deflected. This deflection can be detected by a four quadrant photo-detector and converted into an electrical signal which is measured by a lock-in amplifier (EG&G5210). Through the intermediary of the interfaces of the mechanical chopper and the Look-in amplifier, a microcomputer will set the desired modulation frequency and read the values of the amplitude and phase of the photo-thermal signal and then draw their variations according to the square root modulation frequency.

2.2.2. Theoretical model

The PTD technique consists in heating an absorbing sample using a modulated light pump beam. The optical absorption of the sample will generate a thermal wave that will propagate into the sample and in the surrounding fluid medium, inducing a temperature gradient, and as a consequence, a refractive index gradient in the fluid. A laser probe beam skimming the sample surface and crossing the region with inhomogeneous refractive index gradient is deflected. Its deflection ψ may be related to the thermal properties of the sample and to the temperature T_0 at the sample surface.

Table 2
Deposition conditions.

Coatings	Time of deposition (min)	Bias voltages (-V)		Target power (KW)	Gas mixture (4 μbar)	
		Al	Cr		Ar (%)	N ₂ (%)
Cr	60	0	-900	4	100	0
CrN	60	0	0	//	80	20
CrAlN	60	-300	-900	//	//	//
Cr/CrN	51	//	//	//	//	//
CrN/CrAlN	105	//	//	//	//	//
Cr/CrN/CrAlN	99	//	//	//	//	//

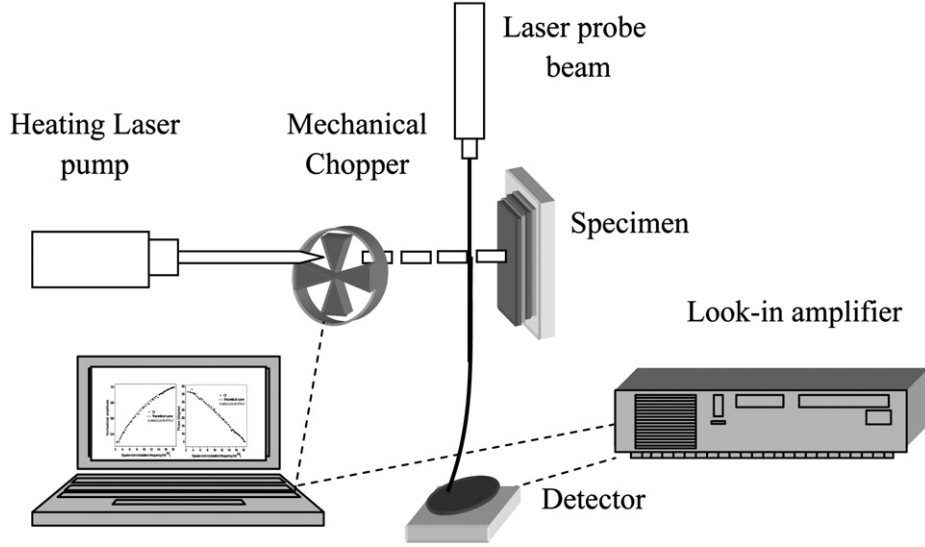


Fig. 2. Schematic experimental setup of the PTD technique.

2.2.3. Deflection calculation

The laser probe beam which passes parallel to the sample surface at a distance x_0 undergoes a periodic deflection as shown in Fig. 3 due to periodic variations of the refractive index of the fluid in the vicinity of the sample. A study of the signal deflection yields a relationship between the amplitude and phase [25,26] of the probe beam deflection ψ as:

$$|\psi| = \frac{\sqrt{2}l}{n\mu_f} \frac{dn}{dT_f} |T_0| e^{-\frac{x}{\mu_f}} \quad (2)$$

$$\varphi = -\frac{x}{\mu_f} + \theta + \frac{5\pi}{4} \quad (3)$$

where l is the width of the pump beam in the direction of the probe laser beam, n , μ_f , and T_f are the refractive index, the thermal

$$T_f(x, t) = T_0 e^{-\sigma_f(x)} e^{j\omega t}$$

$$T_n(x, t) = (X_n e^{\sigma_n(x)} + Y_n e^{-\sigma_n(x)} - Z_n e^{\alpha_n(x)}) e^{j\omega t}$$

$$T_{n-1}(x, t) = (X_{n-1} e^{\sigma_{n-1}(x+l_n)} + Y_{n-1} e^{-\sigma_{n-1}(x+l_n)} - Z_{n-1} e^{\alpha_n(x+l_n)}) e^{j\omega t}$$

$$\vdots$$

$$T_1(x) = (X_1 e^{\sigma_1(x+l_n \dots + l_2)} + Y_1 e^{-\sigma_1(x+l_n \dots + l_2)} - Z_1 e^{\alpha_1(x+l_n \dots + l_2)}) e^{j\omega t}$$

$$T_s(x) = (X_s e^{\sigma_s(x+l_n \dots + l_1)} + Y_s e^{-\sigma_s(x+l_n \dots + l_1)} - Z_s e^{\alpha_s(x+l_n \dots + l_1)}) e^{j\omega t}$$

$$T_b(x, t) = W e^{\sigma_b(x+l_n \dots + l_s)} e^{j\omega t}$$

$$\text{if } 0 \leq x \leq l_f$$

$$\text{if } -l_n \leq x \leq 0$$

$$\text{if } -l_n - l_{n-1} \leq x \leq -l_n$$

$$\text{if } -l_n \dots - l_1 \leq x \leq -l_n \dots - l_2$$

$$\text{if } -l_n \dots - l_s \leq x \leq -l_n \dots - l_1$$

$$\text{if } -l_n \dots - l_s \leq x \leq -l_n \dots - l_1$$

By writing the heat flow expressions in each medium one obtains:

$$\Phi_f(x, t) = K_f \sigma_f T_0 e^{-\sigma_f(x)} e^{j\omega t}$$

$$\Phi_n(x, t) = -K_n \sigma_n \left(X_n e^{\sigma_n(x)} - Y_n e^{-\sigma_n(x)} - \frac{\alpha_n}{\sigma_n} Z_n e^{\alpha_n(x)} \right) e^{j\omega t}$$

$$\Phi_{n-1}(x, t) = -K_{n-1} \sigma_{n-1} \left(X_{n-1} e^{\sigma_{n-1}(x+l_n)} - Y_{n-1} e^{-\sigma_{n-1}(x+l_n)} - \frac{\alpha_{n-1}}{\sigma_{n-1}} Z_{n-1} e^{\alpha_n(x+l_n)} \right) e^{j\omega t}$$

$$\vdots$$

$$\Phi_1(x) = -K_1 \sigma_1 \left(X_1 e^{\sigma_1(x+l_n \dots + l_2)} - Y_1 e^{-\sigma_1(x+l_n \dots + l_2)} - \frac{\alpha_1}{\sigma_1} Z_1 e^{\alpha_1(x+l_n \dots + l_2)} \right) e^{j\omega t}$$

$$\Phi_s(x) = -K_s \sigma_s \left(X_s e^{\sigma_s(x+l_n \dots + l_1)} - Y_s e^{-\sigma_s(x+l_n \dots + l_1)} - \frac{\alpha_s}{\sigma_s} Z_s e^{\alpha_s(x+l_n \dots + l_1)} \right) e^{j\omega t}$$

$$\Phi_b(x, t) = -K_b \sigma_b W e^{\sigma_b(x+l_n \dots + l_s)} e^{j\omega t}$$

$$\text{if } 0 \leq x \leq l_f$$

$$\text{if } -l_n \leq x \leq 0$$

$$\text{if } -l_n - l_{n-1} \leq x \leq -l_n$$

$$\text{if } -l_n \dots - l_1 \leq x \leq -l_n \dots - l_2$$

$$\text{if } -l_n \dots - l_s \leq x \leq -l_n \dots - l_1$$

$$\text{if } -l_n \dots - l_s \leq x \leq -l_n \dots - l_1$$

diffusion length and the temperature of the fluid respectively. φ and θ are the amplitude and phase, respectively, at the temperature T_0 of the sample surface which are function of the thermal properties of the different media, x is the distance between the probe beam axis and the sample surface.

2.2.4. Calculation of the periodic elevation temperature T_0 at the sample surface

We consider the case of a stacking sample formed by n layers on a Si substrate as shown in Fig. 4, where K_i , D_i and l_i are the thermal conductivity, the thermal diffusivity and the thickness of the i th layer, respectively.

The temperature inside each layer is written as:

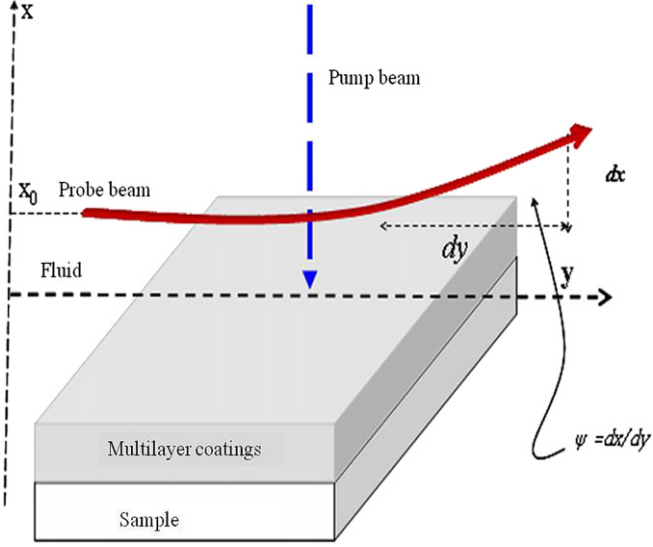


Fig. 3. Schematic representation of the probe beam deflection.

The temperature and heat flow continuity at the different interfaces

$x = 0, x = -l_n, x = -l_n + l_{n-1}, \dots, x = -l_n - l_{n-1} \dots - l_s$ permit to obtain:

The temperature and heat flow continuity at the interface $x = -l_n$ permit to obtain the following equation :

$$\begin{pmatrix} 1 & 1 & -1 \\ 1 & -1 & -r_{n-1} \\ 0 & 0 & E_n/E_{n-1} \end{pmatrix} \begin{pmatrix} X_{n-1} \\ Y_{n-1} \\ E_{n-1} \end{pmatrix} = \begin{pmatrix} e^{-\sigma_n l_n} & e^{\sigma_n l_n} & -e^{-\alpha_n l_n} \\ c_n e^{-\sigma_n l_n} & -c_n e^{\sigma_n l_n} & -c_n r_n e^{-\alpha_n l_n} \\ 0 & 0 & 1 \end{pmatrix} \begin{pmatrix} X_n \\ Y_n \\ E_n \end{pmatrix}$$

$$G_n \begin{pmatrix} X_{n-1} \\ Y_{n-1} \\ E_{n-1} \end{pmatrix} = D_n \begin{pmatrix} X_n \\ Y_n \\ E_n \end{pmatrix}$$

or

$$\begin{pmatrix} X_{n-1} \\ Y_{n-1} \\ E_{n-1} \end{pmatrix} = G_n^{-1} \cdot D_n \begin{pmatrix} X_n \\ Y_n \\ E_n \end{pmatrix} = M_n \begin{pmatrix} X_n \\ Y_n \\ E_n \end{pmatrix}$$

Where

$$G_n = \begin{pmatrix} 1 & 1 & -1 \\ 1 & -1 & -r_{n-1} \\ 0 & 0 & E_n/E_{n-1} \end{pmatrix},$$

$$D_n = \begin{pmatrix} e^{-\sigma_n l_n} & e^{\sigma_n l_n} & -e^{-\alpha_n l_n} \\ c_n e^{-\sigma_n l_n} & -c_n e^{\sigma_n l_n} & -c_n r_n e^{-\alpha_n l_n} \\ 0 & 0 & 1 \end{pmatrix}$$

and

$$M_n = G_n^{-1} \cdot D_n.$$

In the same way we can write in the interface:

Backing	Substrate	Layer (1)	Layer (2)	Layer (i)	Layer (n)	Fluid
---------	-----------	-----------	-----------	-----------	-----------	-------

Fig. 4. Different regions crossed by the heat.

$$x_i = -l_n - l_{n-1} \dots - l_i \begin{pmatrix} X_{i-1} \\ Y_{i-1} \\ E_{i-1} \end{pmatrix} = M_i \begin{pmatrix} X_i \\ Y_i \\ E_i \end{pmatrix}$$

Then

$$\begin{pmatrix} X_1 \\ Y_1 \\ E_1 \end{pmatrix} = M_2 \cdot M_3 \dots M_n \begin{pmatrix} X_n \\ Y_n \\ E_n \end{pmatrix} = \begin{pmatrix} m_{11} & m_{12} & m_{13} \\ m_{21} & m_{22} & m_{23} \\ m_{31} & m_{32} & m_{33} \end{pmatrix} \begin{pmatrix} X_n \\ Y_n \\ E_n \end{pmatrix}$$

In this case we write

$$\begin{cases} X_1 = m_{11}X_n + m_{12}Y_n + m_{13}E_n \\ Y_1 = m_{21}X_n + m_{22}Y_n + m_{23}E_n \end{cases}$$

The writing of the heat flow and temperature continuity at the interfaces $x = 0$ and $x = -l_3 - l_2 - l_1$ give respectively:

$$X_n = \frac{1}{2}(1-g)T_0 + (1+r_3)\frac{E_n}{2}, \quad Y_n = \frac{1}{2}(1+g)T_0 + (1-r_3)\frac{E_n}{2}.$$

And

$$(1-b)e^{-\sigma_1 l_1}X_1 - (1+b)e^{\sigma_1 l_1}Y_1 - (r_1-b)e^{-\alpha_1 l_1}E_1 = 0 \quad (4)$$

Then

$$X_1 = \frac{m_{11}}{2}((1-g)T_0 + (1+r_n)E_n) + \frac{m_{12}}{2}((1+g)T_0 + (1-r_n)E_n) + m_{13}E_n$$

and

$$Y_1 = \frac{m_{21}}{2}((1-g)T_0 + (1+r_n)E_n) + \frac{m_{22}}{2}((1+g)T_0 + (1-r_n)E_n) + m_{23}E_n.$$

Or too

$$X_1 = (m_{11}(1-g) + m_{12}(1+g))\frac{T_0}{2} + (m_{11}(1+r_n) + m_{12}(1-r_n) + 2m_{13})\frac{E_n}{2}$$

and

$$Y_1 = (m_{21}(1-g) + m_{22}(1+g))\frac{T_0}{2} + (m_{21}(1+r_n) + m_{22}(1-r_n) + 2m_{23})\frac{E_n}{2}.$$

That is to say $X_1 = \eta_1 T_0 + \eta_2 E_n$ and $Y_1 = \eta_3 T_0 + \eta_4 E_n$.

By replacing X_1 and Y_1 by its expressions in Eq. (4) one obtains:

$$(1-b)e^{-\sigma_1 l_1}(\eta_1 T_0 + \eta_2 E_n) - (1+b)e^{\sigma_1 l_1}(\eta_3 T_0 + \eta_4 E_n) - (r_1-b)e^{-\alpha_1 l_1}E_1 = 0$$

What gives:

$$\begin{aligned} & ((1-b)\eta_1 e^{-\sigma_1 l_1} - (1+b)\eta_3 e^{\sigma_1 l_1})T_0 \\ & = ((1+b)\eta_4 e^{\sigma_1 l_1} - (1-b)\eta_2 e^{-\sigma_1 l_1})E_n + (r_1-b)e^{-\alpha_1 l_1}E_1 \end{aligned}$$

$$\text{Finally } T_0 = [(1+b)\eta_4 e^{\sigma_1 h_1} - (1-b)\eta_2 e^{-\sigma_1 h_1}] E_n + (r_1 - b) e^{-\alpha_1 h_1} E_1 / [(1-b)\eta_1 e^{-\sigma_1 h_1} - (1+b)\eta_3 e^{\sigma_1 h_1}]$$

$$\text{With } E_i = \alpha_i / 2K_c (\alpha_i^2 - \sigma_i^2).$$

3. Results and discussion

3.1. Characterization of the PVD coatings

According to the EDS + WDS analysis, in the case of multilayer coatings obtained with a two targets, above 20% of nitrogen in the plasma, we obtain a constant atomic composition of 50–52% of N₂, 4–5% of Al, 41–43% of Cr and 3–4% of O₂ (which is negligible) as shown in Table 3. The other deposition parameters (working pressure, deposition time, and target voltage) has been mentioned in Table 2.

Alumina and chromium were used as the reference materials for quantitative analyses. In Table 3, the N/(Cr + Al) ratio varied from 0.95 to 1.2 for all the coatings, which reflects their stoichiometry. Furthermore, the R_a and R_q roughness of the films are low, and their variations do not exceed 4/100 on all surfaces. On the other hand the evolution of the thickness versus the deposition time is always linear.

Fig. 5 shows XRD patterns of the synthesized Cr/CrN/CrAlN and CrN/CrAlN nanoscale multilayers with the same thicknesses (1500 nm). Both the multilayers coatings were crystallized into a rocksalt-type cubic structure. The layers of chromium and CrN coatings in the films are unambiguously identified by the peak (220) to 76.68° and (200) to 51.2°, respectively. The coating has CrN/CrAlN main diffraction peaks [(111) and (200), respectively, at 43.76° and 51.2° characteristics of CrN, compared to the PDF 76-2494, PCPDFWIN Version 2.3, JCPDS-ICDD (2002)] [17,27,28]. One can conclude from the spectra obtained on multilayer coatings Cr/CrN/CrAlN and CrN/CrAlN that the CrN surface layer crystallizes according to the preferred orientation (311) when it crystallizes in volume according to the preferred orientation (200) [2,28–30].

Moreover, the presence of preferred crystallographic orientation is related to the columnar morphology of monolayers Cr, CrN and CrAlN observed by SEM on cross-section as shown in Fig. 6. The growth of the columnar structure perpendicular to the surface is little disturbed at the interfaces between layers. The morphologies of the traditional CrN and nanocomposite CrAlN films (5% of Al content) are studied. It was found that the CrN film exhibited strong columnar structure and no significant difference was observed after alloying with Al. However, the CrAlN film had much smaller grain size (the mean radius of grain is about 12 nm) and denser structure when compared with CrN film deposited under the same conditions [12,31,32]. The dissolving columnar agglomerates were considered resulted from reduced crystallinity due to Al alloying and the formation of an amorphous/crystalline nanocomposite structure. Our results are comparable to those obtained in the work

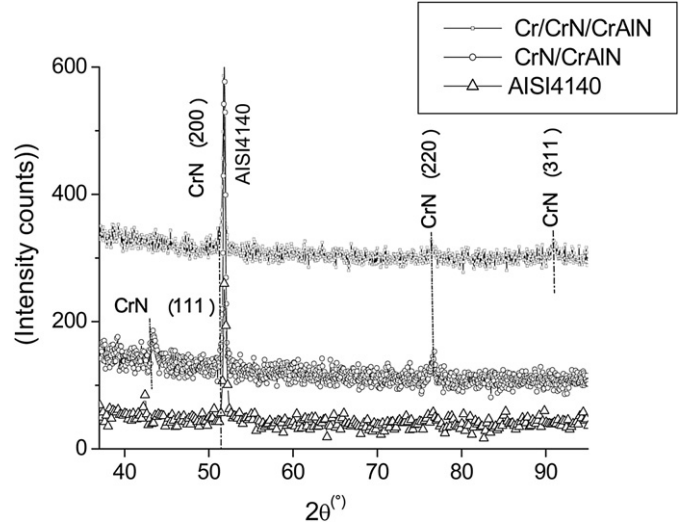


Fig. 5. XRD patterns of uncoated AISI4140 steel and multilayers such as CrN/CrAlN and Cr/CrN/CrAlN on AISI4140 samples.

of Barshilia et al. [31], as well as Okumiya et al. [12] made on the coating CrN/CrAlN.

The results of Wang et al. [32] suggested that the lattice structure of CrAlN films fabricated in this work formed a solid solution whereby Cr atoms were substituted by Al atoms since the covalent radius of Al (0.121 nm) is smaller than that of Cr (0.139 nm). This also caused the shift of the diffraction peaks of the films. In addition, the peak broadening phenomenon and the decrease of the diffraction peaks intensity was also observed with the incorporation of Al in CrN matrix, which could be attributed to the fact that the crystallinity of film correspondingly decreased [32].

In order to investigate the micro-structural changes of CrAlN films, high-resolution TEM observations were performed on CrAlN film as shown in Fig. 7.

From the TEM images for the film CrAlN cross-section (Fig. 7A), it was observed that the coating layer was well grown crystalline phase with relatively regular grain shapes and defects. In addition, it was also found that fine grains about several nanometers were observed in the big grains of this film (Fig. 7B), and at the higher magnification small crystalline grains about some nm (black area distinguished by the lattice fringe contrast) were embedded in the amorphous (white area) matrix.

The XDR and HRTEM investigations detailed above have proved that the incorporation of Al into the CrN matrix led to the formation of a unique nanocomposite microstructures composed of nanocrystallites uniformly embedded in an amorphous matrix. Such formation is based on a strong, thermodynamically driven and diffusion-rate-controlled (spinodal) phase segregation that leads to the formation of stable nanostructures by self-organization [32]. Based on the literature, this amorphous/crystalline nanocomposite

Table 3
Composition, atomic ratios, total thicknesses and roughnesses of the mono and multilayers.

Coatings	N Content (at. %)	Al Content (at. %)	Cr Content (at. %)	Atomic ratio N/(Cr + Al)	Total thickness (nm)	Roughness (μm)	
						Arithmetic roughness (R _a)	Roughness average quadratic (R _q)
Cr	0	0	98	0	860	0.1	0.12
CrN	48	0	51	0.95	690	0.1	0.12
CrAlN	48.2	4	48	1.04	980	0.1	0.12
CrAlN/CrN/Cr	51.8	4.2	42.9	1.2	1500	0.1	0.12
CrAlN/CrN	52	5	41.3	1.2	1500	0.13	0.11

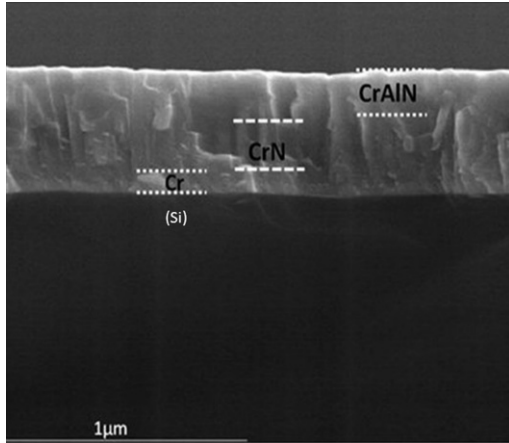


Fig. 6. SEM cross-section observation of a Cr/CrN/CrAlN coated sample.

structure may be favorable to the high performance of mechanical properties owing to the following concepts [32]: (i) combine crystalline and amorphous CrAlN matrix to achieve high hardness with good toughness; and (ii) maintain nanocrystalline size at several nanometer levels to restrict crack and create a large volume of grain boundaries.

Nevertheless, the addition of a third element in the transition metal nitride coating generally increases the residual stress [33]. Therefore, the CrAlN coatings are expected to have higher residual stresses than CrN ones. High internal stresses affect the adhesion of the coatings critically. For this reason thick CrAlN coatings cannot be obtained. These factors led to the exploration of multilayers such as CrN/CrAlN, wherein the properties of CrN and CrAlN can be combined.

Fig. 8 shows that residual stresses in multilayers are lower than the monolayers ones. The reduction of the residual stresses in multilayer coatings compared to those of the monolayers is also mainly due to their interface. The interlayers seem to be effective in absorbing residual stresses during film growth. It's obvious that their values strongly depend on the residual stresses of the monolayers.

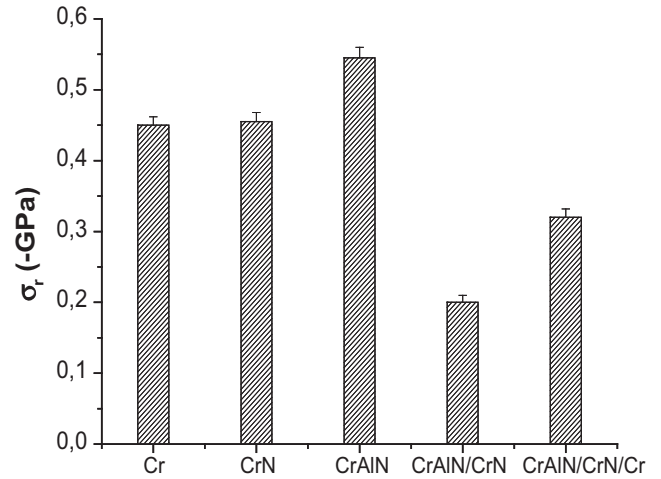


Fig. 8. Residual stress of the films.

3.2. Thermal properties

The determination of the thermal properties of the layers has been made as follows: we started to determine the thermal properties of a chromium layer, and then we studied a sample Cr/CrN coated and determine the thermal conductivity and thermal diffusivity of the CrN layer. After we have understood the thermal properties of the Cr and CrN layers, we could study the thermal properties of CrAlN from the Cr/CrN/CrAlN coated sample.

The AISI4140 steel substrate and the layers have a great optical reflection coefficient that is why they should be covered with a thin graphite layer to absorb the incident light and therefore serve as a heat source. The graphite layer thickness for all samples is 2 μm, its thermal properties and those of the substrate were determined in previous works [18,26].

Fig. 9 shows the experimental and theoretical amplitude and phase variations with the square root modulation frequency of the photo-thermal signal, for the graphite/Cr layers deposited on AISI4140 using the mathematical model of two layers ($n = 2$). The

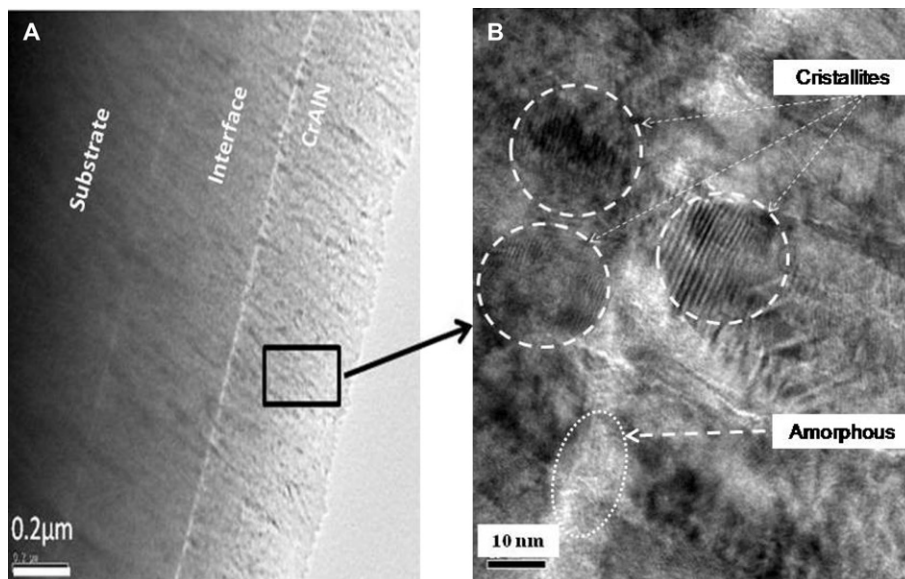


Fig. 7. (A) Cross-section TEM image and (B) HRTEM image of a CrAlN film.

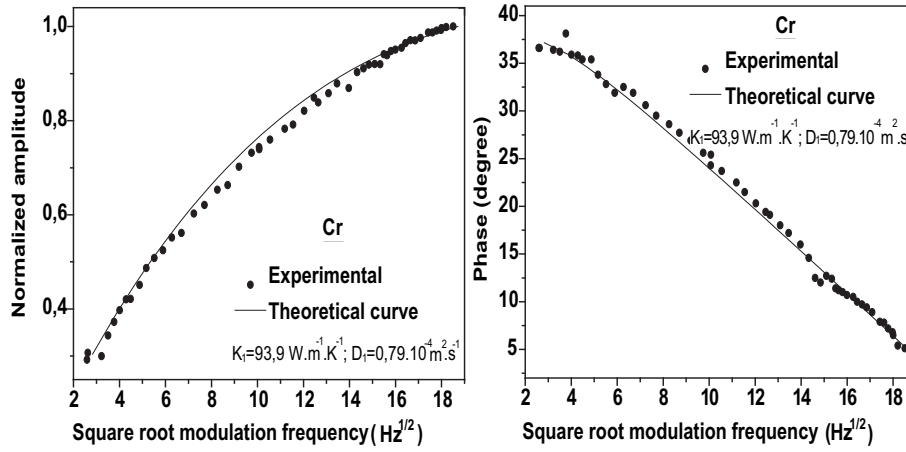


Fig. 9. Normalized amplitude and phase evolution of the photo-thermal signal vs. the square root frequency of the deposited Cr layers.

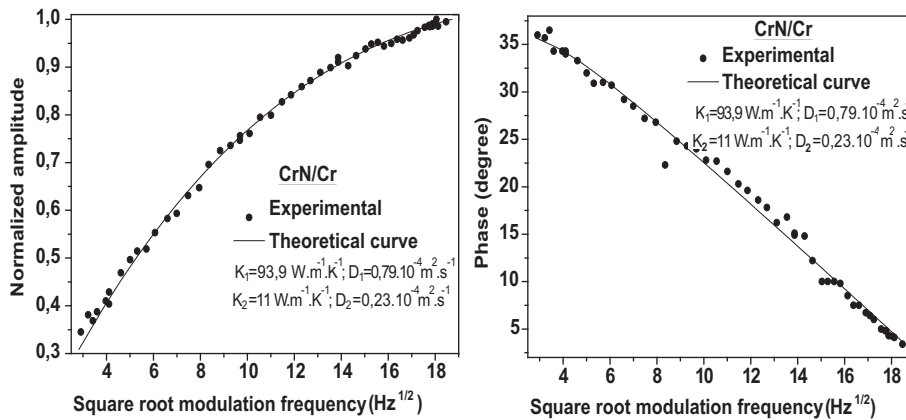


Fig. 10. Normalized amplitude and phase evolution of the photo-thermal signal vs. the square root frequency of the deposited Cr/CrN layers.

best theoretical fit yields a thermal conductivity $K = 93.9 \text{ W m}^{-1} \text{ K}^{-1}$ and thermal diffusivity $D = 0.79 \times 10^{-4} \text{ m}^2 \text{ s}^{-1}$ for the Cr layers.

We purchased our work for the sample composed of steel/Cr/CrN/graphite using the theoretical model for three layers ($n = 3$) whose results are presented in Fig. 10. The thermal conductivity and the thermal diffusivity values obtained are $K = 11 \text{ W m}^{-1} \text{ K}^{-1}$ and $D = 0.23 \times 10^{-4} \text{ m}^2 \text{ s}^{-1}$, respectively. Then we determine the thermal properties of the CrAlN layer deposited on the sample consisting of stacking steel/Cr/CrN/CrAlN/graphite, the curves of

Fig. 11 show that the CrAlN layer presents the following values $K = 2.8 \text{ W m}^{-1} \text{ K}^{-1}$ and $D = 0.052 \times 10^{-4} \text{ m}^2 \text{ s}^{-1}$ of thermal conductivity and diffusivity, respectively.

The thermal conductivity of the coating can be containing a large error due to inaccurate parameters used as input in the calculations. Especially, the coating to substrate thickness ratio is small; the calculated conductivity value will be extremely sensitive to errors in the input parameters. In general, the accuracy of the laser flash technique for two or three layers strongly depends on

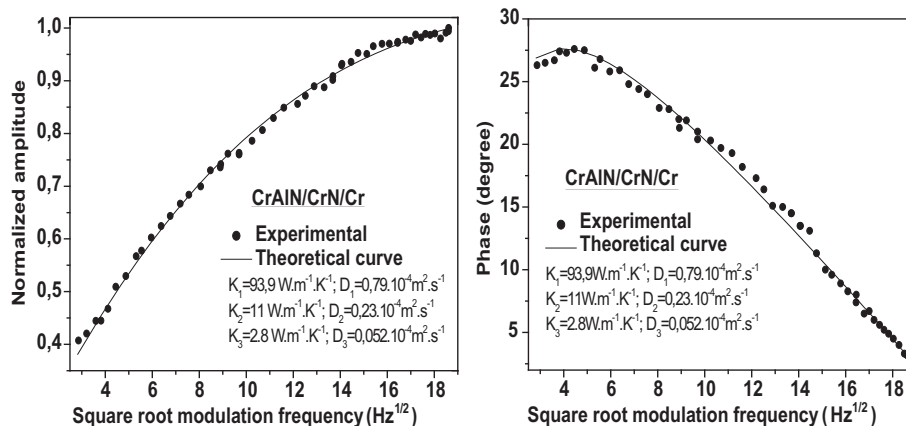


Fig. 11. Normalized amplitude and phase evolution of the photo-thermal signal vs. the square root frequency of the deposited Cr/CrN/CrAlN layers.

Table 4
Thermal properties of the layers.

Layer and substrate	Thermal conductivity ($\text{W m}^{-1} \text{K}^{-1}$)	Thermal diffusivity ($10^{-6} \text{m}^2 \text{s}^{-1}$)	Equivalent thermal conductivity ($\text{W m}^{-1} \text{K}^{-1}$)
AISI4140	26 ± 0.01	9 ± 0.012	
Cr	93.9 ± 0.01	0.79 ± 0.01	
CrN	11 ± 0.015	0.23 ± 0.013	
CrAlN	2.8 ± 0.012	0.052 ± 0.001	
CrN/Cr			13.1 ± 0.012
CrAlN/CrN/Cr			4.6 ± 0.013

possible errors of seven input parameters whereas the accuracy of the thermal diffusivity determined for one layer is only influenced by errors in sample thickness of layer. Therefore, single layers are strongly preferred if high accuracy is needed. Table 4 resumes the thermal properties of the different layers taken separately and of the equivalent thermal conductivity of the stacked films given, respectively, by:

$$\frac{1}{K_e} = \frac{1}{e_{\text{Cr}} + e_{\text{CrN}}} \left(\frac{e_{\text{Cr}}}{K_{\text{Cr}}} + \frac{e_{\text{CrN}}}{K_{\text{CrN}}} \right)$$

for the stacking Cr/CrN and

$$\frac{1}{K_e} = \frac{1}{e_{\text{Cr}} + e_{\text{CrN}} + e_{\text{CrAlN}}} \left(\frac{e_{\text{Cr}}}{K_{\text{Cr}}} + \frac{e_{\text{CrN}}}{K_{\text{CrN}}} + \frac{e_{\text{CrAlN}}}{K_{\text{CrAlN}}} \right)$$

for the stacking Cr/CrN/CrAlN.

In a model developed by Ghrib et al. [25,26] the overall coating conductivity results from the combined effect of these two zones (amorphous and crystallites). Essential parts of this two-zone model were modified in this work describing the total thermal resistance of a coating as a series combination of the thermal resistance of the inner zone and of the outer zone, providing a good agreement between model and measured data.

We note from the values summarized in Table 4 that the CrAlN layer has lower thermal properties compared with the Cr and CrN layers, so it can act as a thermal insulator. The conductivity value of CrAlN is extremely low compared to those of the monolayer of Cr and CrN. This is well known and can be explained by the columnar microstructure which is characterized by elongated inter-columnar pores that are predominantly aligned perpendicular to the plane of the coating [34,35]. In the CrAlN layer, the heat flow is mainly parallel to these inter-columnar gaps, the heat transfer is not effectively reduced. However, the primary columns exhibit a feathery structure with inter-columnar pore [36]. These fine inter-columnar gaps contribute to a moderate reduction in the thermal conductivity as they are generally inclined to the heat flow. For that reason, the thermal conductivity of CrN coatings is still significantly lower than the thermal conductivity of the fully dense Cr layer. This result suggests that the structure of the Cr and CrN coating near the interface to the metallic substrate has a markedly different thermal conductivity. Structural differences of Cr/CrN/CrAlN and Cr/CrN PVD multilayers can be roughly divided into two zones, the fine-grained inner zone (Cr/CrN film) and the coarse columnar outer zone (CrAlN coating). The thermal conductivity of the fine grain inner zone is much higher than the thermal conductivity of the outer zone. This effect is attributed to the higher grain boundary density as well as numerous oblique columnar boundaries in the outer zone [37]. Thus, the thermal conductivity is dominated by phonon scattering at defect/grain boundaries in this part of the coating, and this results in a lower conductivity of around $2.5 \text{ W m}^{-1} \text{K}^{-1}$ at room temperature. Moreover, the decreased thermal conductivity of Cr/CrN/CrAlN multilayers is attributed to the increased total porosity resulting from an increase in the

number of interface pores associated with the formation of non-uniform interfaces between layers, which causes increased phonon scattering.

4. Conclusion

The physico-chemical, mechanical and thermal properties of different nitride-based coatings obtained by PVD have been determined, taking into consideration their microstructure. CrN and CrAlN coatings deposited on AISI4140 substrates exhibited B1 NaCl structure with (200) reflection of cubic phase. The CrN/CrAlN and Cr/CrN/CrAlN multilayers also exhibited a prominent reflection along (200) planes.

Moreover, the present work reports experimental and theoretical results on the thermal properties (conductivity and diffusivity) and residual stress of Cr, CrN, CrAlN, Cr/CrN and Cr/CrN/CrAlN thin layers.

1. In light of various experimental investigation. It was found that the thermal conductivity values determined on monolayers and substrate are generally higher or equal than to the multilayer coatings.
2. We compare the values of thermal conductivity obtained from the two multilayer Cr/CrN and Cr/CrN/CrAlN, it is clear that the latter coating has the lowest value.
3. The thermal conductivity of nanoscale thin film is remarkably lower than that of bulk materials because of its various size effects.
4. The obtained CrAlN coatings structure is porous and they present columnar grains containing many nanopores. The thermal conductivity of the coatings depended on the number and composition of the layers they consisted in. As a result the decrease of the thermal conductivity of multilayers is due to the increase in their total porosity resulting from the introduction of large numbers of pores between layers compared to a single layer, which is related to the nature of the non-uniform interface and inter-phases between layers. The increased porosity results in an increase in phonon scattering, which decreases the mean free path for phonon transport through the coating.

As a conclusion, the CrAlN and Cr/CrN/CrAlN coatings with their low thermal conductivity can be used as thermal barrier on a tool surface and therefore minimize crack-causing alternating stresses.

Acknowledgments

The authors wish to thank the Regional Council of Burgundy and EGIDE for their financial support, and also the technical staff of the Arts et Métiers ParisTech of Cluny: especially Romaric Masset and Pierre-Michel Barbier for the samples preparation.

References

- [1] Chiba Y, Omura T, Ichimura H. *J Mater Res* 1993;8:1109.
- [2] Bin T, Xiaodong Z, Naisai H, Jiawen H. *Surf Coat Technol* 2000;131:391.
- [3] Sue JA, Chang TP. *Surf Coat Technol* 1995;76–77:61.
- [4] Barshilia HC, Rajam KS. *Bull Mater Sci* 2003;26:233.
- [5] Barshilia HC, Jain A, Rajam KS. *Vacuum* 2004;72:241.
- [6] Barshilia HC, Prakash MS, Jain A, Rajam KS. *Vacuum* 2005;77:169.
- [7] W Grips VK, Ezhil Selvi V, Barshilia HC, Rajam KS. *Electrochem. Acta* 2006;51:3461.
- [8] Barshilia HC, Rajam KS. *Surf Coat Technol* 2004;183:174.
- [9] Barshilia HC, Prakash MS, Poojari A, Rajam KS. *Thin Solid Films* 2004;460:133.
- [10] Barshilia HC, Rajam KS, Sridhara Rao DV. *Surf Coat Technol* 2006;200:4586.
- [11] Barshilia HC, Rajam KS, Jain A, Gopinadhan K, Chaudhary S. *Thin Solid Films* 2006;503:158.
- [12] Okumiya M, Griepentrog M. *Surf Coat Technol* 1999;112:123.
- [13] Mayrhofer PH, Willmann H, Mitterer C. *Surf Coat Technol* 2001;146–147:222.

- [14] Wuhrer R, Yeung WY. *Scr Mater* 2004;50:1461.
- [15] Kawate M, Hashimoto AK, Suzuki T. *Surf Coat Technol* 2003;165:163.
- [16] Brizuela M, Luis AG, Braceras I, Onate JJ, Lopez JCS, Martinez DM, et al. *Surf Coat Technol* 2005;200:192.
- [17] Uchida M, Nihira N, Mitsuo A, Toyoda K, Kubota K, Aizawa T. *Surf Coat Technol* 2004;177–178:627.
- [18] Ghrif T, Bejaoui F, Hamdi A, Yacoubi N. *Thermochim Acta* 2008;473(1–2):86–91.
- [19] Baragetti S, La Vecchia GM, Terranova A. *Int J Fatigue* 2005;27:1541.
- [20] Nordin M, Larsson M, Hogmark S. *Surf Coat Technol* 1998;106:234.
- [21] Wang Q, Ishikawa H, Nakano S, Ogiso H, Akedo J. *Vacuum* 2004;75:225–9.
- [22] Ghrif T, Tlili B, Nouveau C, Benlatreche Y, Lambertin M, Yacoubi N, et al. *Phys Proc* 2009;2:1327–36.
- [23] Murphy JC, Aamodt LC. *J Appl Phys* 1980;51:4580.
- [24] Jackson WB, Amer NM, Boccara AC, Fournier D. *Appl Opt* 1981;20:1333.
- [25] Ghrif T, Salem SB, Noureddine Y. *Tribol Int* 2009;42(3):391.
- [26] Ghrif T, Yacoubi N, Saadallah F. *Sens Actuat A* 2007;135:346.
- [27] Nouveau C, Djouadi M, Marchal Rémy, Lambertin Michel. *Méc Ind* 2002;3:333.
- [28] Musil J, Hrubý H. *Thin Solid Films* 2000;365:104.
- [29] Kim YJ, Byun TJ, Han JG. *Superlattices Microstruct* 2009;45:73.
- [30] Barshilia HC, Rajam KS. *J Appl Phys* 2005;98:014311.
- [31] Barshilia CHarish, Deepthi B, Selvakumer N, Jain A, Rajam KS. *Appl Surf Sci* 2007;253:5076.
- [32] Wang L, Guangan Z, Wood RJK, Wang SC, Xue Q. *Surf Coat Technol* 2010;204:3517–24.
- [33] Vingsbo O, Hogmark S, Jönsson B, Ingemarson A. *American society for testing and materials, Philadelphia*; 1986, p. 257.
- [34] Chen L, Du Y, Wang SQ, Li J. *Int J Refract Metals Hard Mater* 2007;25:400.
- [35] Chunyan Y, Linhai T, Yinghui W, Shebin W, Tianbao L, Bingshe X. *Appl Surf Sci* 2009;255:4033.
- [36] Lin J, Mishra B, Moore JJ, Sproul WD, Rees JA. *Surf Coat Technol* 2007;201:6960.
- [37] Rätzer-Scheibe H-J, Schulz U, Krell T. *Surf Coat Technol* 2006;200:5636.